Chinese Chemical Letters 33 (2022) 2171–2177

Contents lists available at ScienceDirect

Chinese Chemical Letters

journal homepage: www.elsevier.com/locate/cclet

Self-sacrificial template synthesis of Fe, N co-doped porous carbon as efficient oxygen reduction electrocatalysts towards Zn-air battery application

Tianfang Yang, Ye Chen, Yang Liu, Xupo Liu*, Shuyan Gao*

School of Materials Science and Engineering, Henan Normal University, Xinxiang 453007, China

ARTICLE INFO

Article history:
Received 26 June 2021
Revised 20 July 2021
Accepted 2 September 2021
Available online 8 September 2021

Keywords:
Electrocatalyst
Oxygen reduction reaction
Fe
N co-doped porous carbon
Fe-N active sites
Zn-air batteries

ABSTRACT

Designing highly efficient non-precious based electrocatalysts for oxygen reduction reaction (ORR) is of significance for the rapid development of metal-air batteries. Herein, a hydrothermal-pyrolysis method is employed to fabricate Fe, N co-doped porous carbon materials as effective ORR electrocatalyst through adopting graphitic carbon nitride (g-C_3N_4) as both the self-sacrificial templates and N sources. The g-C_3N_4 provides a high concentration of unsaturated pyridine-type N to coordinate with iron to form Fe-N active sites. Through adjusting the Fe doping amounts, it is proved that appropriate Fe doping content is conducive to the construction of abundant defects and active sites of Fe-N. The as-prepared catalyst exhibits superior electrocatalytic ORR performance in alkaline media with half-wave potential ($E_{1/2}$ = 0.82 V) and onset potential (E_{onset} = 0.95 V), equivalent to the commercial Pt/C catalyst. Moreover, there is almost no activity loss after 10 k continuous cyclic voltammetry cycles and methanol tolerance, indicating the excellent durability and superior methanol tolerance. Remarkably, when assembled as the cathode in a Zn-air battery, the device displays a power density of 99 mW/cm^2, an open-circuit potential of 1.48 V and long-term discharge-charge cycling stability, indicating the promising potential to substitute the Pt catalyst for practical application.

In view of the current energy dilemma and environmental pollution, the progress of sustainable and clean energy is the key research direction at present [1,2]. Zn-air batteries (ZABs) are identified as one of the most promising next-generation energy equipment on account of the high safety factor, inexpensive, excellent durability and impressive theoretical specific energy density [3,4]. For ZABs, the oxygen reduction reaction (ORR) is a fundamental reaction occurred on the cathode [5]. However, the sluggish kinetics of ORR has restricted the extensive implementation of ZABs [6]. Currently, platinum-group-metal (PGM) catalysts are widely utilized as the electrocatalysts for ORR owing to the excellent catalytic performance [7]. Unfortunately, the high cost, serious scarcity and long-term instability have hindered the large-scale application of PGM catalysts [8,9]. Therefore, the investigation of inexpensive and effective non-PGM catalysts for ORR is significant for promoting the rapid development of ZABs [10].

Recent advances have demonstrated that some non-PGM catalysts including metal oxides, sulfides, carbides and nitrides can be adopted as high-performance ORR catalysts, especially transition metal-nitrogen-carbon catalysts (M-N-C) [11]. The M-N-C composite catalysts (especially Fe-N-C) have been reported as the potential alternatives to the PGM for boosting ORR due to the relatively low cost, prominent catalytic activity and excellent durability [12,13]. More importantly, the nitrogen dopant atoms (particularly pyridinic-N and pyrrolic-N) feature high affinity to the transition metals, thereby forming the M-N active sites as the oxygen adsorption and reduction centers, which drastically improves the electrocatalytic performance [14]. In this regard, it is of critical importance to manipulate the electronic interaction by adjusting the type of nitrogen. Therefore, choosing appropriate nitrogen sources is beneficial for regulating the ORR property of M-N-C catalysts [15]. Besides, the strategies of optimizing the pore structure and constructing high specific surface area are also conducive to improving the ORR activity [16]. Generally, the template method is usually used to prepare porous materials, such as applying the templates of SiO_2 nanospheres, styrene spheres and metal oxides. However, this pore-making process is always cumbersome and toxic and the employed hydrofluoric acid could etch and poison the crucial M-N active sites [17,18]. Therefore, it is necessary to develop the new facil approach to fabricate efficient porous

* Corresponding authors.
E-mail addresses: liuxupo@htu.edu.cn (X. Liu), shuyangao@htu.cn (S. Gao).

https://doi.org/10.1016/j.cclet.2021.09.014
1001-8417/

M-N-C materials for promoting the progress of ORR electrocatalysts.

Herein, a facile hydrothermal-pyrolysis method is employed to fabricate Fe, N co-doped porous carbon materials (NPC-Fe_x) as high-performance ORR electrocatalyst. The graphitic carbon nitride (g-C_3N_4) that is non-metallic semiconductor polymer material with graphite structure has been adopted as both the self-sacrificial templates and N sources. The high concentration of unsaturated pyridine-type N in g-C_3N_4 provides rich lone pair electrons trap metal ions in the ligands to form abundant and uniform Fe-N active sites. In addition, using g-C_3N_4 as templates cannot only enlarge the specific surface area of carbon materials, but also eliminate the complicated steps of traditional template methods. The as-prepared NPC-$Fe_{0.3}$ catalyst exhibits splendid electrocatalytic property with the half-wave potential ($E_{1/2}$ = 0.82 V) and onset potential (E_{onset} = 0.95 V), superior stability as well as high methanol tolerance. Moreover, the assembled ZAB with the NPC-$Fe_{0.3}$ catalyst contains the maximum power density of 99 mW/cm^2 and extraordinary durability, demonstrating better property than the Pt/C-based device. It reveals the promising application of the ORR catalyst as supersedes for Pt/C within energy conversion equipment.

The Fe, N co-doped porous carbon materials (NPC-Fe_x, x represents the mass of iron precursors) were synthesized through a facile hydrothermal-pyrolysis process (Scheme 1). For comparison, the PC-Fe sample was synthesized without g-C_3N_4, while NPC was synthesized without iron(III) 2,4-pentanedionate. Firstly, the g-C_3N_4 was achieved by the thermal condensation of melamine in air. The XRD pattern of g-C_3N_4 exhibits the in-plane repeating motifs of the continuous heptazine networks (100) and interlayer stacking of aromatic segments (002) at 12.9° and 27.5°, respectively (Fig. S1 in Supporting information) [19]. Then, the hydrothermal treatment was carried out after thoroughly stirring with glucose as the carbon sources, g-C_3N_4 as the nitrogen sources and iron(III) 2,4-pentanedionate as the metal sources. Therein, Fe atoms were concomitantly immobilized in the frameworks to form Fe/g-C_3N_4@C precursors since the g-C_3N_4 could provide the rich unsaturated N atoms as the anchoring sites. Finally, the Fe, N co-doped porous carbon materials (NPC-Fe_x) were obtained by pyrolysis of Fe/g-C_3N_4@C precursors at 900°C in N_2 atmosphere. Notably, the g-C_3N_4 could also be employed as the templates for pore-making. The TGA curve shows that the thermal decomposition of g-C_3N_4 begins at 550 °C until the complete disintegration at 750°C (Fig. S2 in Supporting information), consistent well with the previous literature [20]. During this process, the gas molecules produced by the g-C_3N_4 escape from the carbon materials, which are expected to generate abundant pores in the carbon materials.

The prepared samples of NPC-$Fe_{0.3}$ and NPC show a broad characteristic diffraction peak at 22.6°, which is assigned to the (002) plane of graphitic carbon. There is no peak corresponding to metallic Fe or other iron compounds (Fig. 1a). Meanwhile, some obvious signals in the ranges of 20°-30° and 40°-50° are determined for PC-Fe, matching well with the characteristic peaks of FeC and Fe_3C phases. It is speculated that the absence of Fe_3C and FeC characteristic peaks in NPC-$Fe_{0.3}$ is attributed to the fact that Fe is mainly coordinated with the N species in g-C_3N_4. Raman spectroscopy was performed to characterize the chemical structure and the degree of structural defects of NPC-$Fe_{0.3}$. There are two typical peaks located at 1350 cm^{-1} (D band) and 1580 cm^{-1} (G band) (Fig. 1b). The D band corresponds to the disordered sp^3 carbon (on behalf of defects and disorder-induced features), whereas the G band denotes the graphitic sp^2 carbon. Moreover, The defect level of carbon-based materials was studied by the intensity ratio of D band to G band (I_D/I_G) [21]. As revealed in Fig. 1b, the relative intensity ratio of NPC-$Fe_{0.3}$ (I_D/I_G = 1.31) is much higher than that of PC-Fe (I_D/I_G = 1.18), indicating that more defects are generated in the graphitic carbon lattices owing to the addition of nitrogen atoms [22]. Actually, the index (I_D/I_G) of NPC-$Fe_{0.3}$ is lower than that of NPC (I_D/I_G = 1.33) due to the catalysis effect of iron can promote the graphitization of carbon [23]. Furthermore, NPC-$Fe_{0.3}$ exhibits a typical 2D peak at about 2700 cm^{-1} belonging to the typical peak of graphene-based material, further indicating the graphene structure of catalysts [24]. The specific surface area and pore size distribution were characterized by nitrogen gas adsorption/desorption isotherms. All the samples reveal a classic type-IV curve with an H4-type hysteresis loop at the relatively higher relative pressure, demonstrating the existence of a large amount of mesopores (Fig. 1c). The curves of pore size distribution further reveal the mesoporous structure and the pore sizes of NPC-$Fe_{0.3}$ are mainly centered at ~11.4, ~15.6 and ~26.1 nm (the insert in Fig. 1c). Generally, the mesopores can improve specific surface area, afford numerous active sites and facilitate the transfer and diffusion of ORR related species (O_2 and *OH, *etc.*) [25]. Compared to PC-Fe, NPC-$Fe_{0.3}$ exhibits more abundant porous structures toward large sizes and broad distributions, further confirming the favorable pore-making role of g-C_3N_4. The Brunauer–Emmett–Teller (BET) specific surface area of NPC-$Fe_{0.3}$ is 224.4 m^2/g, which is much larger than the specific surface area of PC-Fe (162.9 m^2/g). It is speculated that the large specific surface area and hierarchical porous structure of NPC-$Fe_{0.3}$ are attributed to the following reason: the thermal decomposition of g-C_3N_4 releases corrosive gas to etch the carbon matrix, which acts as the templates to create abundant mesopores, thus increasing the specific surface area [26].

FT-IR spectra were conducted to analyze the functional groups of catalysts (Fig. 1d). The peak located at ~3433 cm^{-1} corresponds to the -OH stretching vibration [24], while the peaks of C-H stretching vibration are located at ~2920 and ~1460 cm^{-1}, respectively. The peaks at ~1626, ~1548, ~1420, ~1084 and ~1052 cm^{-1} are attributed to C=O, C-N, C-N, C-O and C-O-C vibrations, respectively [27]. Moreover, a new peak appears for NPC-$Fe_{0.3}$ at ~880 cm^{-1} after the introduction of iron precursors, which can be attributed to the Fe-N stretching vibration [28]. However, in the absence of metal precursors or g-C_3N_4, there is no Fe-N bonds for NPC and PC-Fe. The above results indicate that nitrogen and oxygen doping is obviously observed in the NPC-$Fe_{0.3}$, which is beneficial for improving the contact performance between the electrode materials and electrolytes. In addition, the existence of Fe-N bonds can effectively improve the ORR performance. The sample of NPC-$Fe_{0.3}$ has been selected to explore the structure of catalysts. The SEM image reveals that NPC-$Fe_{0.3}$ presents a gossamer lamellar structure with rich wrinkles (Fig. 1e), which is profitable for the exposion of active sites and mass transportation [29]. In addition, PC-Fe sample without g-C_3N_4 has a large number of uniform nanospheres due to the hydrothermal reaction of glucose (Fig. S3a in Supporting information), while NPC shows a similar appearance to NPC-$Fe_{0.3}$ (Fig. S3b in Supporting information). The above results clearly indicate that the presence of g-C_3N_4 in the synthesis process promotes the formation of lamellar structure with wrinkles. The lamellar frameworks of NPC-$Fe_{0.3}$ were further ascertained by the TEM image (Fig. 1f). The HR-TEM image (Fig. 1g) demonstrates the lattice fringes of 0.34 nm matching well with the (002) crystal plane of graphitic structure [30]. The selected area electron diffraction (SAED) pattern exhibits a blurred ring resulted from the poor crystallinity of the N-doped carbon substrate (the insert in Fig. 1g). The EDS element mappings of NPC-$Fe_{0.3}$ show that the C, N, O and Fe atoms are uniformly distributed throughout the structure (Fig. 1h), revealing that Fe and N elements are successfully incorporated into carbon materials. The above results sufficiently prove that NPC-$Fe_{0.3}$ is rich of N- and O-functional groups and Fe-N bonds, which is conducive to improving the hydrophilicity. The water contact angle is 2.5° for NPC-$Fe_{0.3}$ by the water contact angle test (Fig. 1i and Fig. S4 in Supporting information), which is sig-

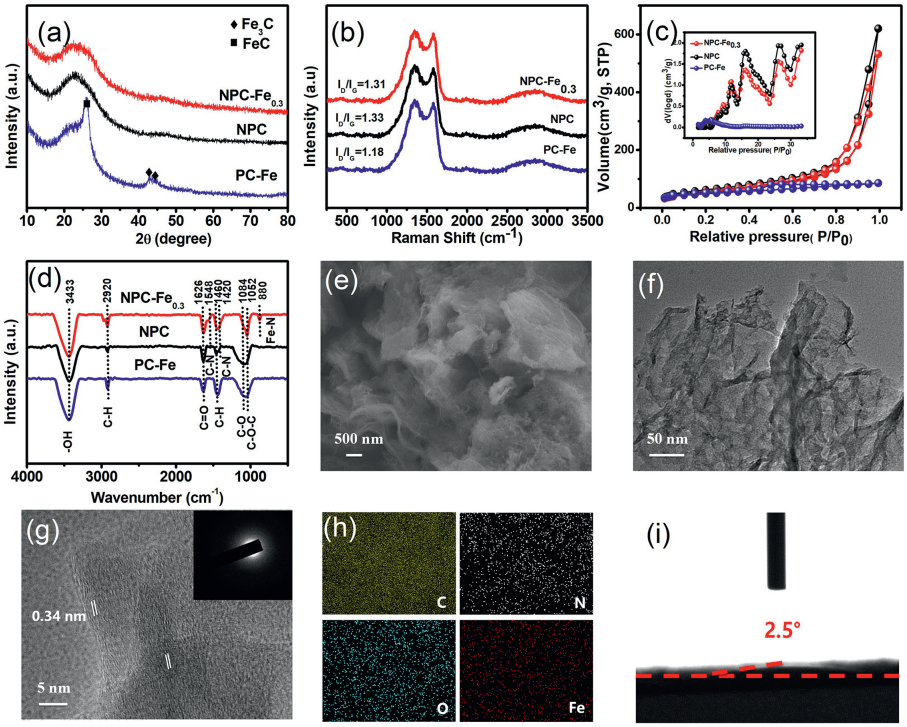

Fig. 1. (a) XRD patterns. (b) Raman spectra. (c) nitrogen gas adsorption-desorption isotherms (the insert is pore-size distribution). (d) FT-IR spectra of NPC-$Fe_{0.3}$, NPC and PC-Fe. (e) FE-SEM image. (f) TEM image. (g) HR-TEM image (insert is SAED pattern). (h) EDS mapping images of C, N, O and Fe elements. (i) contact angle of NPC-$Fe_{0.3}$.

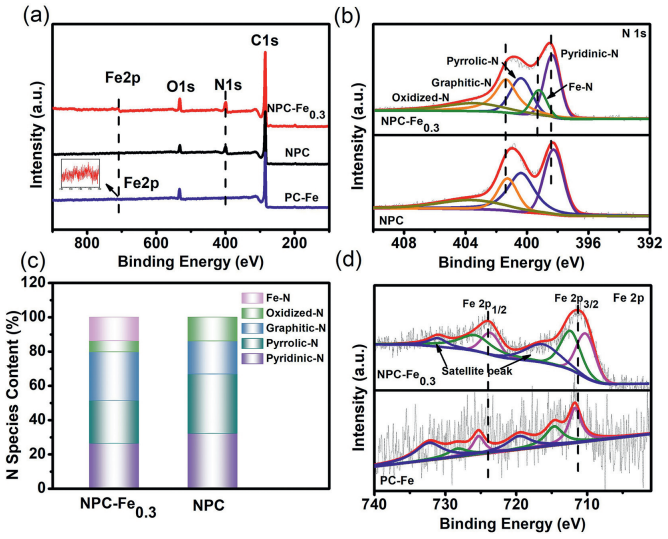

Fig. 2. (a) XPS survey spectra of NPC-$Fe_{0.3}$, NPC and PC-Fe. (b) N 1s spectra of NPC-$Fe_{0.3}$ and NPC. (c) The contents of various N configurations for NPC-$Fe_{0.3}$ and NPC. (d) Fe 2p spectra of NPC-$Fe_{0.3}$ and PC-Fe.

nificantly much smaller than that of PC-Fe (8.2°) and NPC (13.6°), indicating a super hydrophilicity [25].

XPS determination was carried out to analyze the compositions and chemical states. The survey spectra (Fig. 2a) have indicated that Fe and N elements are successfully doped into the carbon skeleton for NPC-$Fe_{0.3}$. For comparison, the sample of PC-Fe was synthesized without the addition of g-C_3N_4. However, due to the lack of N element coordination with iron ions in PC-Fe, the metal cannot be anchored effectively and part of Fe combines with C to form FeC and Fe_3C nanoparticles. Some nanoparticles are easily removed in the pickling process, resulting in a low content. Fe signal of PC-Fe is much weaker than that of NPC-$Fe_{0.3}$ according to XPS spectra. The high-resolution C 1s spectrum of NPC-$Fe_{0.3}$ in Fig. S5a (Supporting information) can be fitted into C=C, C–C, C–N and O–C=O bonds at 284.6, 285.3, 286.5 and 289.1 eV, respectively [27]. The high-resolution O 1s spectrum of NPC-$Fe_{0.3}$ (Fig. S5b in Supporting information) exhibits four different O species, which are assigned to C=O (531.0 eV), C–OH (532.3 eV), C–O–C (533.2 eV) and O–C=O (534.7 eV), respectively [31]. The N 1s XPS spectrum of NPC-$Fe_{0.3}$ in Fig. 2b can be separated into five peaks of pyridinic-N (398.3 eV), pyrrolic-N (400.6 eV), graphitic-N (401.5 eV), oxidized-N (405.0 eV) and the apparent peak at 399.2 eV corresponding to Fe-N bonds [12,28], which is an available evidence for the presence of Fe-N bonds in NPC-$Fe_{0.3}$. Importantly, a positive shift of pyridinic-N and graphitic-N relative to NPC in NPC-$Fe_{0.3}$ is about 0.2 eV due to the modified Fe atoms and Fe-N bonds. It suggests that the electronic metal-support interaction between Fe atoms and g-C_3N_4. The g-C_3N_4 provides a high concentration of unsaturated pyridine-type N to coordinate with iron to form Fe-N active sites. The high concentration of unsaturated pyridinic-type N in g-C_3N_4 affords rich electron lone pairs for trapping metal ions in the ligands, leading to the relevant charge transfer and changes of the binding energy of Fe and N species [32,33]. Moreover, the relative contents of Fe-N, pyrrolic-N, oxidized-N, pyridinic-N and graphitic-N species of NPC-$Fe_{0.3}$ and NPC are calculated from the XPS spectra (Fig. 2c and Table S1 in Supporting information). Although the N content decreases after doping Fe atoms, the percentage of Fe-N increases up to 13.8%. In addition to forming Fe-N bonds, the doped Fe atoms also facilitate the conversion of pyrrolic-N and oxidized-N to graphitic-N, which is conductive to promote the ORR activity [34]. Furthermore, the high proportions of pyridinic-N and pyrrolic-N have been confirmed to increase the π state density, spin density and current density of C atoms around the Fermi level, consequently promoting the ORR performance [35]. Recent advances have proved that the N configuration (pyridinic-N, pyrrolic-N or graphitic-N) is the key aspect to the electrocatalytic activity

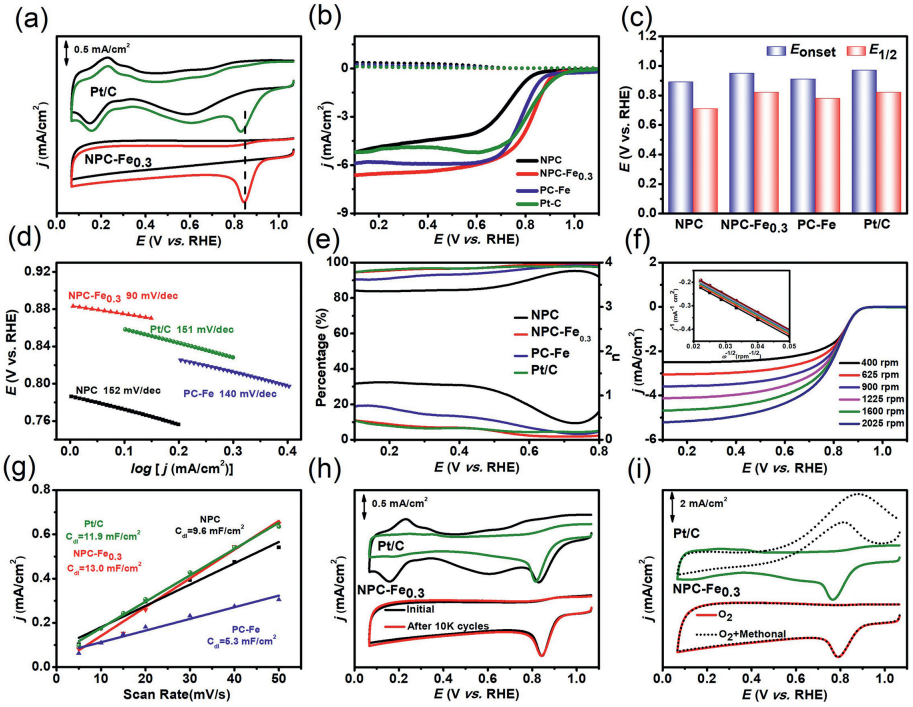

Fig. 3. Electrocatalytic behavior in 0.1 mol/L KOH: (a) CV curves of NPC-$Fe_{0.3}$ and Pt/C. (b) LSV curves. (c) comparison of $E_{1/2}$ and E_{onset}. (d) Tafel plots. (e) H_2O_2 yields and electron numbers of NPC, NPC-$Fe_{0.3}$, PC-Fe and Pt/C. (f) LSV curves of NPC-$Fe_{0.3}$ with a sweep rate of 10 mV/s at different rotating speeds ranging from 400 rpm to 2025 rpm (the insert is K-L plots in different potentials). (g) plots extraction. (h) stability tests. (i) resistance of methanol crossover of NPC-$Fe_{0.3}$ and Pt/C.

of nitrogen-doped carbon materials. The pyridinic-N and graphitic-N possess superior electron-accepting abilities to absorb oxygen, while the pyrrolic-N and pyridinic-N tend to form the metal coordination structure (Fe-N), which is reported to be the effective active sites of Fe, N co-doped porous carbon materials [28,36].

The spectra of Fe 2p (Fig. 2d) can be deconvolved into two main peaks, which are assigned to Fe $2p_{3/2}$ and Fe $2p_{1/2}$, respectively [11]. It is found that the Fe $2p_{3/2}$ binding energy region shows two peaks at 710.1 and 712.2 eV, which are assigned to the $2p_{3/2}$ of the Fe (II) and Fe(III) ions, respectively [13]. Meanwhile, the peaks at 723.7 and 725.8 eV are attributed to the binding energy of the $2p_{1/2}$ orbitals of the Fe(II) and Fe(III) species, respectively [37]. The peaks at 716.2 eV and 731.2 eV stand for the corresponding satellite peaks [38]. Based on the analysis, the peak at 710.1 eV in the Fe $2p_{3/2}$ XPS spectrum of NPC-$Fe_{0.3}$ indicates that Fe ions are coordinated with pyridinic-N to form Fe-N bonds, which can accelerate O_2 adsorption and $4e^-$ reduction to enhance ORR activity [39]. As expected, the high-resolution Fe 2p XPS spectrum also confirms the absence of metallic Fe in the NPC-$Fe_{0.3}$ and Fe mainly exists in the ionic states of Fe(III) and Fe(II). Additionally, it is obvious that the slight negative shifts of Fe $2p_{3/2}$ and Fe $2p_{1/2}$ are observed for NPC-$Fe_{0.3}$ compared with PC-Fe. According to the d electron catalysis theory, the d electron orbital property of transition metals is one of the core factors affecting the intrinsic activity of catalytic active sites [40]. The transition metal Fe has a strong ability to form coordination compounds with ligands due to the existence of empty orbitals in the outer d orbital. Therefore, Fe is easy to coordinate with the unsaturated pyridine type N in g-C_3N_4, which is stable in the cavity formed by the three heptazine rings [41]. The results are consistent with the N 1s spectra analysis, indicating that the interaction between Fe and N is conducive to the stable adsorption of O_2 and intermediates (*OH) [42].

The ORR performances were determined through a common three-electrode system in 0.1 mol/L KOH. As shown in Fig. 3a and Fig. S6 (Supporting information), there is a quasi-rectangular without O_2 reduction peak in N_2 condition, while a distinct O_2 reduction peak appears at about 0.845 V in the CV curves of NPC-$Fe_{0.3}$ in O_2-saturated electrolyte, which is 18 mV more positive than that of the commercial Pt/C. The electrochemical impedance spectra (EIS) are analyzed based on the equivalent circuit diagram (Fig. S7 in Supporting information). The equivalent series resistance (R_s) and interfacial charge transfer (R_{ct}) values of NPC-$Fe_{0.3}$ are 1.9 Ω and 60.7 Ω, respectively. The low inherent resistance of electrolyte facilitates ions diffusion. The Warburg resistance (R_p) for NPC-$Fe_{0.3}$ is only 0.36 Ω, demonstrating the fast ion diffusion velocity [43,44]. The LSV curves were recorded on RRDE to further illustrate the ORR activity. Fig. 3b shows that NPC-$Fe_{0.3}$ displays the prominent ORR activity in terms of E_{onset} (0.95 V) and $E_{1/2}$ (0.82 V), which are superior to those of NPC (E_{onset} = 0.89 V, $E_{1/2}$ = 0.71 V) and PC-Fe (E_{onset} = 0.91 V, $E_{1/2}$ = 0.78 V), confirming that the introduction of iron and nitrogen is imperative to facilitate the ORR activity of carbon materials. It is worth noting that the $E_{1/2}$ values of NPC-$Fe_{0.3}$ is comparable to Pt/C (E_{onset} = 0.97 V, $E_{1/2}$ = 0.82 V) and exceeds most of the reported catalysts (Fig. 3c and Table S2 in Supporting information). Moreover, the limiting current density (j_L) of NPC-$Fe_{0.3}$ is 6.5 mA/cm^2, which is 1.3-fold higher than that of Pt/C, evidencing a superior ORR activity.

Tafel slope is a crucial parameter to evaluate the ORR activity. The Tafel slope of NPC-$Fe_{0.3}$ is 90 mV/dec, which is the smallest among all the determined samples (Fig. 3d), indicating a rapid ORR kinetic process. Meanwhile, the corresponding RRDE measurements were also employed to calculate the yields of hydrogen peroxide (H_2O_2%) and the electron transfer numbers (n) (Fig. 3e). In the potential range from 0 to 0.80 V, the H_2O_2 yield remains below 10% and the n values of NPC-$Fe_{0.3}$ are 3.80–4.00, similar to that of Pt/C. Therefore, the prepared NPC-$Fe_{0.3}$ catalyst exhibits superior ORR activity with a desirable four-electron reaction pathway. Furthermore, the RDE measurements were conducted at various rotating speeds changing from 400 rpm to 2025 rpm to investigate the catalyst kinetics of NPC-$Fe_{0.3}$ (Fig. 3f). As the rotational speed

increases, the diffusion-limiting current density of NPC-$Fe_{0.3}$ gradually increases with the reduction of O_2 diffusion distance. The K-L plots of NPC-$Fe_{0.3}$ in the inset of Fig. 3f display good linearity and parallelism between j^{-1} and $\omega^{-1/2}$, suggesting the first-order reaction kinetics toward the dissolved O_2 concentration. According to the K-L plots, the electron transfer number is calculated to be 3.8–4.0, further proving the $4e^-$ dominant process. Besides, the electrochemical active surface area (ECSA) was calculated by the electrochemical double-layer capacitance (C_{dl}), which was obtained from the CV curves in the absence of O_2 (Fig. 3g and Fig. S8 in Supporting information). The C_{dl} of NPC-$Fe_{0.3}$ is 13.0 mF/cm^2, which is much higher than those of NPC (9.6 mF/cm^2), PC-Fe (5.3 mF/cm^2) and Pt/C (11.9 mF/cm^2), indicating the excellent accessibility [45,46].

Excellent durability and methanol tolerance are also crucial for ORR electrocatalysts. The durability of NPC-$Fe_{0.3}$ has been investigated by cycling the electrode in 0.1 mol/L KOH at an accelerated scan rate of 50 mV/s in O_2-saturated. As depicted in Fig. 3h, after 10 k continuous cyclic voltammetry cycles, the peak potential is almost identical to the original one, much better than that of Pt/C. The unobvious decay demonstrates the brilliant durability of NPC-$Fe_{0.3}$ towards ORR, which is attributed to the large graphitization degree of carbon matrix. It can availably strengthen the carbon corrosion resistance, improving the operating stability of catalysts. In addition, the resistance of methanol crossover has been tested by injecting 1 mL 1.0 mol/L methanol into the electrolyte during the CV test. As shown in Fig. 3i, the obvious methanol poisoning effect containing a distinct methanol redox peak and a significant current drop are observed for Pt/C, whereas the current response of NPC-$Fe_{0.3}$ barely decays upon the addition of CH_3OH. The consequence demonstrates that NPC-$Fe_{0.3}$ exhibits more excellent tolerance to the methanol than Pt/C catalyst. By making a preliminary summary, NPC-$Fe_{0.3}$ possesses superior stability and selectivity towards ORR in alkaline electrolyte, which can be regarded as a promising electrocatalyst for practical application.

Furthermore, the influence of Fe contents on structures and electrocatalytic performances has been investigated by synthesizing a series of Fe, N co-doped porous carbon materials. XRD patterns in Fig. S9 (Supporting information) exhibit that the excess Fe dopants lead to the serious agglomeration of metal sites to form numerous FeC and Fe_3C nanoparticles. As revealed in Fig. S10 (Supporting information), the calculated I_D/I_G values are 1.27, 1.30, 1.31, 1.15 and 1.08 for NPC-$Fe_{0.1}$, NPC-$Fe_{0.2}$, NPC-$Fe_{0.3}$, NPC-$Fe_{0.4}$ and NPC-$Fe_{0.5}$, respectively. With the increased iron doping amounts, the defect degree appears a trend of first increase and then decrease. The defects can modulate the surface state of the electronic structure (charge and spin densities) and greatly affect the adsorption of intermediates related to ORR process, thereby enhancing the ORR activity [47]. The nitrogen adsorption/desorption isotherms of all samples present a typical IV type curve and the pore size distribution trend is also similar, indicating that the Fe contents have no significant effect on the surface area and pore size distribution (Fig. S11 in Supporting information). The survey XPS spectra (Fig. S12 in Supporting information) indicate that the Fe and N elements are successfully doped into the carbon skeletons. As shown in Table S3 (Supporting information), the highest Fe contents are found when the doping amount is 0.3 g. When the doping amounts continue to increase, the Fe contents show a downward trend. The excessive Fe dopants lead to the serious agglomeration of metal sites to form numerous FeC and Fe_3C nanoparticles, which can be removed during the acid leaching process. The loss of nanoparticles results in a decrease in the Fe contents of NPC-$Fe_{0.4}$ and NPC-$Fe_{0.5}$. Therefore, the higher Fe contents are conducive to forming abundant Fe-N active sites, further promoting the oxygen reduction activity. Furthermore, the ORR activity of electrocatalysts with different Fe contents was evaluated by the CV measurements. NPC-$Fe_{0.3}$ shows a smaller semicircle than other catalysts in the Nyquist plot (Fig. S13 in Supporting information), demonstrating a fast charge transfer efficiency. As depicted in Fig. S14a (Supporting information), the oxygen reduction potential of NPC-$Fe_{0.3}$ is the most positive among these catalysts, which is much higher than those of other catalysts. As can be observed from the LSV curves in Fig. S14b (Supporting information), NPC-$Fe_{0.3}$ affords the best catalytic activity with E_{onset} of 0.95 V and $E_{1/2}$ of 0.82 V, much higher than those of NPC-$Fe_{0.1}$ (E_{onset} = 0.91 V, $E_{1/2}$ = 0.79 V), NPC-$Fe_{0.2}$ (E_{onset} = 0.92 V, $E_{1/2}$ = 0.80 V), NPC-$Fe_{0.4}$ (E_{onset} = 0.90 V, $E_{1/2}$ = 0.79 V) and NPC-$Fe_{0.5}$ (E_{onset} = 0.90 V, $E_{1/2}$ = 0.78 V). In addition, NPC-$Fe_{0.3}$ manifests the greatest advantage in H_2O_2 yield, electron transfer number, Tafel slope and electrochemical active area (Figs. S14c–e and S15 in Supporting information). Remarkably, the effect of Fe doping contents on ORR activity follows a "volcano plot" trend (Fig. S14f in Supporting information), which is consistent with the trend of the defect degree of the carbon materials (Table S3). It further proves that the defects influence the ORR activity of carbon-based catalysts. The activity is continuously accelerated as the Fe doping increases up to 0.3 g and then decreases with the larger Fe doping. This phenomenon manifests that the lower doping generates insufficient active sites, whereas the higher doping results in the formation of FeC and Fe_3C nanoparticles as well as unfavorable carbon structure (*i.e.*, fewer defects). Therefore, it proves that the active sites of iron species serve as a significant role in the process of promoting ORR activity.

To further explore the practical application of NPC-$Fe_{0.3}$, the primary ZAB with NPC-$Fe_{0.3}$ as the air cathode and Zn foil as the anode were assembled in 6.0 mol/L KOH and 0.2 mol/L $Zn(OAc)_2$ (Fig. 4a). Accordingly, the ZAB assembled by the commercial 20 wt% Pt/C was also conducted in the similar condition. As a result, the open-circuit voltage (VOC) of NPC-$Fe_{0.3}$ is 1.48 V, whereas the battery based on Pt/C only exhibits the voltage of 1.45 V (Fig. 4b). As demonstrated in Fig. 4c, the power density of the NPC-$Fe_{0.3}$-based ZAB reaches a maximum of 99 mW/cm^2 at 150 mA/cm^2, which exceeds the Pt/C-based device (82 mW/cm^2 at 125 mA/cm^2). Moreover, two series-connected NPC-$Fe_{0.3}$-based ZABs can power 69 red LEDs (in the inset of Fig. 4c), demonstrating the potential application of the prepared catalysts in practical energy equipment. Besides, the current density is further altered between 5 mA/cm^2 and 100 mA/cm^2 to assess the stability of cycle discharge performance. The discharge voltages for the NPC-$Fe_{0.3}$-based ZAB are maintained higher than that of Pt/C-based battery with the increasing current density, especially at high current density (Fig. 4d). Notably, the discharge voltage can also be maintained after lowering the current density to the origin low value, indicating the excellent discharge stability and rate capability of the NPC-$Fe_{0.3}$ derived ZAB [48]. Furthermore, to evaluate the stability of the ZABs, the galvanostatic discharge-charge cycling curves are obtained with a constant current density of 5 mA/cm^2 in Fig. 4e. The NPC-$Fe_{0.3}$-based ZAB exhibits exceptionally high cycle stability with negligible voltage decay over 145 h. Therefore, the as-prepared NPC-$Fe_{0.3}$ sample can be employed within ZABs as a high-efficiency and durable catalyst.

In summary, a facile hydrothermal-pyrolysis approach is employed to fabricate Fe, N co-doped porous carbon materials as highly efficient ORR electrocatalyst through adopting g-C_3N_4 as both the self-sacrificial templates and N sources. The unsaturated pyridinic-type N with a single component in g-C_3N_4 is applied to combine with iron to form rich Fe-N active sites. Employing g-C_3N_4 as templates can also effectively increase the specific surface area of carbon materials. Through systematically studying the Fe doping amounts, we emphasize that the abundant defects and adequate Fe-N active sites are critical for promoting the ORR property of catalysts. Owing to these factors, the as-prepared NPC-$Fe_{0.3}$ catalyst exhibits superior ORR performances in the alkaline solu-

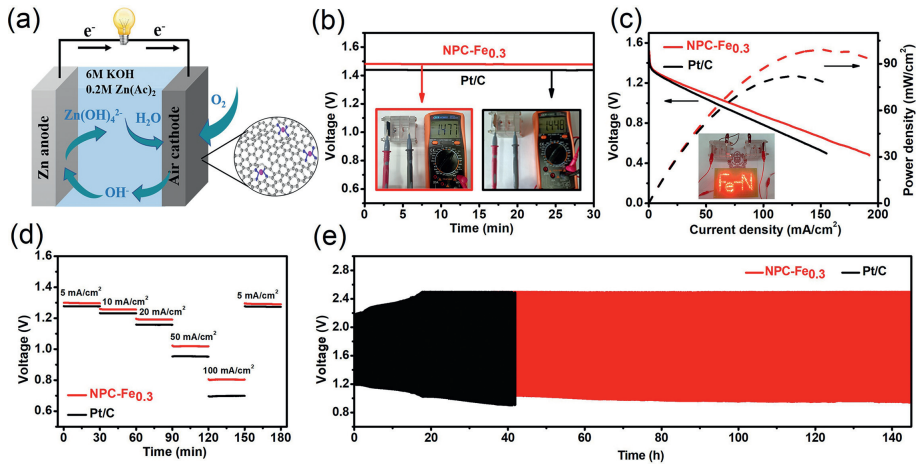

Fig. 4. (a) Schematic diagram of the Zn-air battery. (b) The open-circuit voltage. (c) The polarization curves and corresponding power density plots (inset is the photograph of 69 red LED powered by two ZABs in series with NPC-$Fe_{0.3}$ as the air cathode). (d) Galvanostatic discharge curves with different current densities from 0 to 100 mA/cm^2. (e) The voltage-capacity curves of ZABs at 5 mA/cm^2 assembled with NPC-$Fe_{0.3}$ and commercial Pt/C.

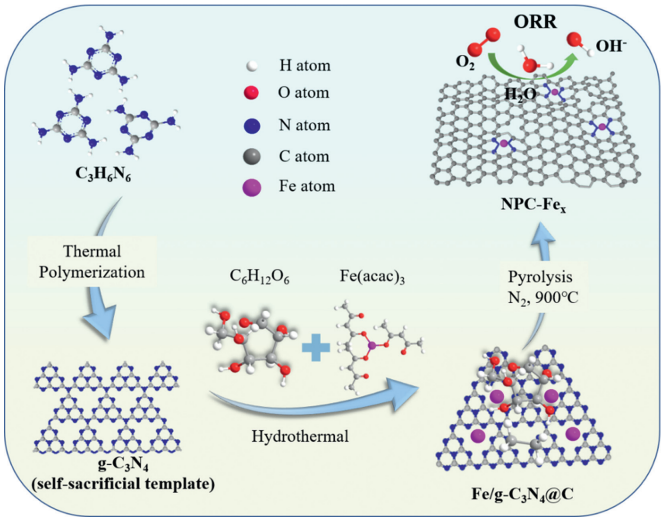

Scheme 1. Schematic illustration of preparing NPC-Fe_x catalysts through a facile hydrothermal-pyrolysis process.

tion with onset potential (E_{onset} = 0.95 V) and half-wave potential ($E_{1/2}$ = 0.82 V), as well as low Tafel slope, low H_2O_2 yield and quick 4-electron transfer ORR pathway. At the same time, NPC-$Fe_{0.3}$ exhibits prominent durability and methanol tolerance. Furthermore, when adopted as the air electrode, the assembled ZAB delivers a power density of 99 mW/cm^2 and superior durability over 145 h. This work provides valuable ideas for the research and progress of high-performance non-noble metal-based ORR electrocatalysts in both energy conversion and storage applications.

Declaration of competing interest

The authors declare that they have no known competing financial interests or personal relationships that could have appeared to influence the work reported in this paper.

Acknowledgments

This work was supported by the National Natural Science Foundation of China (Nos. U1804255 and 51872076), the Program for Innovative Research Team of Henan Scientific Committee (No. CXTD2014033), the Project of Central Plains Science and Technology Innovation Leading Talents, Henan Province (No. 194200510001) and the Scientific and Technological Research Project, Henan province (No. 212102210651).

Supplementary materials

Supplementary material associated with this article can be found, in the online version, at doi:10.1016/j.cclet.2021.09.014.

References

[1] S. Chu, Y. Cui, N. Liu, Nat. Mater. 16 (2016) 16–22.
[2] G. Ren, S. Chen, J. Zhang, J. Mater. Chem. A 9 (2021) 5751–5758.
[3] J. Song, S. Qiu, F. Hu, Adv. Funct. Mater. 31 (2021) 2100618.
[4] D. Ji, L. Fan, L. Li, Adv. Mater. 31 (2019) 1808267.
[5] S. Fu, C. Zhu, J. Song, Adv. Energy Mater. 7 (2017) 1700363.
[6] X.X. Wang, M.T. Swihart, G. Wu, Nat. Catal. 2 (2019) 578–589.
[7] X. Luo, X. Wei, H. Wang, ACS Sustain. Chem. Eng. 8 (2020) 9721–9730.
[8] J. Guo, C.Y. Lin, Z. Xia, Angew. Chem. Int. Ed. 57 (2018) 12567–12572.
[9] J. Liu, D. Zhu, Y. Zheng, ACS Catalysis 8 (2018) 6707–6732.
[10] X. Han, X. Ling, Y. Wang, Angew. Chem. Int. Ed. 58 (2019) 5359–5364.
[11] Z. Huang, H. Pan, W. Yang, ACS Nano 12 (2018) 208–216.
[12] Y. Zhou, Y. Yu, D. Ma, ACS Catal. 11 (2020) 74–81.
[13] L. Zong, X. Chen, S. Dou, Chin. Chem. Lett. 32 (2021) 1121–1126.
[14] P. Su, W. Huang, J. Zhang, Nano Res. 14 (2020) 1069–1077.
[15] D. Zhao, K. Sun, W.C. Cheong, Angew. Chem. Int. Ed. 59 (2020) 8982–8990.
[16] Z. Qiao, H. Zhang, S. Karakalos, Appl. Catal. B: Environ. 219 (2017) 629–639.
[17] H. Zeng, W. Wang, J. Li, ACS Appl. Mater. Interfaces 10 (2018) 8721–8729.
[18] Q.L. Zhu, W. Xia, T. Akita, Adv. Mater. 28 (2016) 6391–6398.
[19] G. Lei, W. Zhao, L. Shen, Appl. Catal. B: Environ. 267 (2020) 118663.
[20] Y. Li, J. Gao, F. Zhang, J. Mater. Chem. A 6 (2018) 15523–15529.
[21] Y. Ren, H. Wang, T. Zhang, Chin. Chem. Lett. 32 (2021) 2243–2248.
[22] D. Yu, Y. Ma, F. Hu, Adv. Energy Mater. (2021) 2101242.
[23] Z. Tan, H. Li, Q. Feng, J. Mater. Chem. A 7 (2019) 1607–1615.
[24] C. Chen, Y. Zhu, M. Tian, Nano Energy 81 (2021) 105623.
[25] Y. Zhao, X. Li, X. Jia, Nano Energy 58 (2019) 384–391.
[26] H. Yu, L. Shang, T. Bian, Adv. Mater. 28 (2016) 5080–5086.
[27] M. Tian, Y. Zhu, Y. Chen, Nano Energy 83 (2021) 105825.
[28] C. Guo, R. Zhou, Z. Li, Micropor. Mesopor. Mat. 303 (2020) 110281.
[29] D. Liu, C. Wu, S. Chen, Nano Res. 11 (2018) 2217–2228.
[30] X. Li, B.Y. Guan, S. Gao, Energy Environ. Sci. 12 (2019) 648–655.
[31] Y. Zhu, C. Chen, M. Tian, Nano Energy 83 (2021) 105720.
[32] J. Yang, W. Li, D. Wang, Adv. Mater. 32 (2020) 2003300.
[33] Y. Zheng, Y. Jiao, Y. Zhu, J. Am. Chem. Soc. 139 (2017) 3336–3339.
[34] X. Ao, W. Zhang, Z. Li, ACS Nano 13 (2019) 11853–11862.
[35] X. Liu, W. Yang, L. Chen, ACS Appl. Mater. Interfaces 12 (2020) 4463–4472.
[36] S. Yi, X. Qin, C. Liang, Appl. Catal. B: Environ. 264 (2020) 118537.
[37] Y. Li, H. Huang, S. Chen, Nano Res. 12 (2019) 2774–2780.
[38] P. Shi, X. Cheng, S. Lyu, Chin. Chem. Lett. 32 (2021) 1210–1214.
[39] Y. Zang, H. Zhang, X. Zhang, Nano Res. 9 (2016) 2123–2137.
[40] C. Cui, Y. Liu, S. Mehdi, Appl. Catal. B: Environ. 265 (2020) 118612.

[41] Z. Chen, J. Zhao, C.R. Cabrera, Small Methods 3 (2018) 1800368.
[42] X. Han, T. Zhang, W. Chen, Adv. Energy Mater. 11 (2020) 1800368.
[43] X. Han, X. Ling, D. Yu, Adv. Mater. 31 (2019) 1905622.
[44] Z. Zhang, X. Li, C. Zhong, Angew. Chem. Int. Ed. 59 (2020) 7245–7250.
[45] S. Peng, F. Gong, L. Li, J. Am. Chem. Soc. 140 (2018) 13644–13653.
[46] X. Zheng, X. Han, Y. Cao, Adv. Mater. 32 (2020) 2000607.
[47] J. Zhang, J. Zhang, F. He, Nano-Micro Lett. 13 (2021) 65.
[48] J. Yang, L. Chang, H. Guo, J. Mater. Chem. A 8 (2020) 1229–1237.